RESEARCH ARTICLE

INTERNATIONAL RESEARCH JOURNAL OF MULTIDISCIPLINARY TECHNOVATION

Asian Research Association

DOI: 10.54392/irjmt2642

Bi_2O_3-Incorporated V_2O_5 Nanocomposite: Enhanced Structural, Optical, and Electrochemical Properties for Supercapacitor Applications

P. Jency Sebatine [a], R. Mohan Kumar [a, *], S. Sherin Celshia [b], K. Arul varman [c], S. Muthamizh [b, *]

[a] Department of Physics, Presidency College Chennai 600005, Tamil Nadu, India.
[b] Department of Physiology, Saveetha Dental College & Hospitals, Saveetha Institute of Medical & Technical Sciences, Saveetha University, Chennai - 600077, Tamil Nadu, India.
[c] Department of Physics & Nanotechnology, SRM Institute of Science & Technology, Kattankulathur-603203, Tamil Nadu, India.
* Corresponding Author Email: mohan66@hotmail.com, muthamizh23@ymail.com

DOI: https://doi.org/10.54392/irjmt2642

Received: 16-03-2026; Revised: 26-05-2026; Accepted: 31-05-2026; Published: 08-06-2026

Abstract: The present work is an attempt to explore the impact of bismuth oxide (Bi_2O_3) at different concentrations (5%, 10%, and 15%) on the structural, optical, and electrochemical features of hydrothermally synthesized V_2O_5 nanoparticles. Structure characterization via X-ray diffraction (XRD) confirmed that the orthorhombic phase of V_2O_5 remains in all composite samples, with slight changes caused by Bi_2O_3. The study of optical properties involved DRS-UV, and the results pointed to the band-gap gradual increase, notably for 15 % Bi_2O_3 sample. The shape changes as well as the particle distribution changes due to the composite formation were confirmed by FE-SEM-EDX. XPS study showed that the pure V_2O_5 chemical environment had been changed after the addition of Bi2O3. Electrochemical evaluations, achieved by cyclic voltammetry and charge-discharge cycling, revealed considerable improvements in capacitance as well as stability. The 15% Bi_2O_3/V_2O_5 nanocomposite electrode demonstrated exceptional cycling durability with the largest specific capacitance (487 F g^{-1} at 1 A g^{-1}), and outstanding retention of 89% after 5000 cycles among the investigated concentrations. The assembled asymmetric device with 15% Bi_2O_3/V_2O_5 nanocomposite and activated carbon attained an exceptional energy density of 38.4 Wh kg^{-1} and a power density of 16,000 W kg^{-1}.

Keywords: Vanadium Pentoxide (V_2O_5), Bismuth oxide, Nanocomposite, Structural Properties, Supercapacitors, Energy Storage.

1. Introduction

Electrochemical measurements by means of cyclic voltammetry and charge-discharge cycling revealed significant improvements in capacitance and stability where the sample 15 % Bi_2O_3/V_2O_5 exhibited the most optimized performance in terms of energy storage efficiency and cycling durability. The findings reported here confirm that bismuth oxide is a feasible method to alter V_2O_5 properties for enhanced supercapacitor devices [1]. Compared to other storage systems, supercapacitors have become attractive alternatives because of their unique combination of high power density, fast charge and discharge, long cycle life, and safe operation [2]. However, the relatively low energy density of supercapacitors still remains as one of the major limitations that impedes their use to be widely spread in high-performance applications. To resolve this problem, the development of advanced electrode materials with tailored structural and electronic properties has become the central research avenue [3]. Transition metal oxides (TMOs) are very promising to be used as electrode materials of supercapacitors as they are the main source of pseudocapacitance in these materials that originate from fast and reversible Faradaic redox reactions. Among the TMOs, vanadium pentoxide (V_2O_5) is the most promising due to its very high theoretical capacitance (~294 mF cm^{-2}), capacity of being switched easily in multiple oxidation states ($V^{5+}/V^{4+}/V^{3+}$), and layered structure which facilitates the intercalation of the charge carriers. Moreover, V_2O_5 is plentiful, cheap, and non-toxic, thus making it even more attractive for large-scale energy storage applications [4]. However, even with these advantages, V_2O_5 by itself faces major drawbacks because of its low intrinsic electrical conductivity (around 10^{-2} to 10^{-3} S/cm), its structural instability upon cycling, and its slow ion diffusion kinetics, which in general, limit its application as a supercapacitor electrode severely [5].

To address these limitations, various strategies have been investigated, including morphology control [6], nanostructuring [7], and composite formation with conductive agents such as carbon nanotubes or graphene, and metal oxide composite [8]. Among these, composite stands out as a highly effective method to tune the physicochemical properties of V_2O_5 without significantly altering its host structure [9]. Composite can significantly improve the performance of a material in several ways like enhancing the conductivity, creating oxygen vacancies, changing the band structure, increasing the electrochemical activity, and stabilizing the lattice during repetitive cycling. Many research works have been conducted to look into the effects of composite with transition metal oxides and rare-earth metals (like Cu, Bi, Fe, Mn, Ce, and Yb) on V_2O_5, which have uncovered major improvements in the electrochemical performance, optical absorption, and mechanical stability of the material [10]. Bismuth oxide composite is just about the most overlooked-techniques that can change the properties of V_2O_5 in a very impressive way. The Bi^{3+} ions have a larger ionic radius (1.03 Å) than V^{5+} (0.59 Å), thus when they are mixed into the V_2O_5 crystal structure, lattice distortion and expansion are induced [11]. The spacing between the layers is widened as a result of this expansion, which is therefore beneficial because it facilitates ion diffusion and makes the electrolyte more accessible. Moreover, the single Bi^{3+} cation is expected to generate oxygen vacancies and electronic defects that are key factors in increasing both the charge storage and the conductivity [12]. Moreover, Bismuth has unique electronic features due to the 6s2 lone pair electrons that can participate in charge transfer processes and increase redox activity. These changes in the structure and electronics, in fact, work together to elevate the performance of V_2O_5 in energy storage devices [13]. Various recent studies have been showing the benefits of Bi or similar dopants in oxide systems more and more. A case in point is the research carried out on Bi-doped TiO_2 and ZnO, which resulted in the suggestion of increased oxygen vacancies concentrations, narrowed band gaps, and enhanced conductivity [14, 15]. Similar phenomena have been observed in vanadium oxides when Cu and Ce doped, leading to an increase in oxygen vacancies, decrease in crystallite sizes, and better pseudocapacitance [16]. These examples point to the possibility that Bismuth oxide composite of V_2O_5 may yield similar or even better results. In addition, the fact that Bi is a non-toxic and chemically stable element makes it even more favourable for its use in eco-friendly energy storage systems [17]. On the molecular level, the merging of Bi can significantly alter the crystal morphology and the grain boundaries of V_2O_5 nanoparticles. The changes in the crystal structure and the lattice of the material due to the presence of substitution sites create areas in the material that are distorted and, therefore, may be responsible for the increase in the surface area and the number of active sites that can take part in the electron transfer reactions [18]. X-ray diffraction (XRD) analyses of doped V_2O_5 usually show peak broadening, this is indicative of a decrease in crystallite size as well as an increase in microstrain, therefore, both these factors are enhancing surface reactivity and electrolyte interaction [19]. Such nano scaled modifications do not only promote kinetic of the electrode but also serve as a volume change buffer during cycling, thereby the durability is increased. As far as optics are concerned, the Bismuth oxide composite can change the electronic band structure of V_2O_5 thus resulting in the change of its band gap [20]. Ultraviolet-visible (UV-Vis) absorption spectroscopy analyses usually reveal red-shifts of the absorption edge of doped V_2O_5, which is indicative of band gap gradual increase and an increased ability of the material to absorb light. Even though this characteristic is mainly required for photocatalytic applications, it can also be linked to an increased carrier concentration and improved electrical conductivity in supercapacitors. [21, 22] Such improvements, at least in part, can be attributed to the higher electrical conductivity and faster reaction kinetics caused by composite formation. Electrochemical tests of doped V_2O_5 and both the fundamentally key figures of specific capacitance, energy density, and rate capability are, in many instances, improved noticeably due to extended redox activity and enhanced conductivity. Comparing to pure V_2O_5, Cu-doped V_2O_5 showed a specific capacitance value that was 2–3 times higher with positive results in charging-discharging rates as well as cycle stability [23, 24]. It is anticipated that a Bismuth oxide composite will result similar enhancement in the properties, mainly due to the ability to generate more oxygen vacancies and tune the electronic structure in a more effective way. In addition, the Bi redox-active feature can also promote pseudocapacitance, thus leading to a higher energy storage capacity. On the synthesis side, Bismuth-doped V_2O_5 nanoparticles may be prepared via various wet-chemical routes like sol-gel, hydrothermal, or solvothermal methods [25-27]. such methods allow correct control of composite concentration, particle size, and morphology. Further crystallinity and more uniform defect distribution can result from post-synthesis operations such as annealing.

In this research, the bismuth oxide composite with vanadium pentoxide was realized by the hydrothermal route and characterized by XRD, FT-IR, DRS-UV, and Raman to determine the crystalline characteristics, functional groups, and optical properties, respectively. FE-SEM were used for the morphological study, and XPS was employed to reveal the chemical environment of the compound. The present work demonstrates that Bi_2O_3 incorporation into V_2O_5 creates a defect-rich hetero-interface with enhanced oxygen-vacancy concentration and mixed-valence electronic structure, leading to improved charge-transfer kinetics and superior asymmetric supercapacitor performance. The novelty of the present work lies not merely in the

hydrothermal synthesis route, but in the defect-engineered Bi_2O_3/V_2O_5 heterostructure that promotes oxygen-vacancy formation, mixed-valence states, and enhanced electrochemical charge-transfer kinetics for asymmetric supercapacitor applications.

2. Materials and Method

2.1 Materials

Chemicals such as Bismuth (II) Nitrate pentahydrate $Bi(NO_3)_3{\cdot}5H_2O$, oxalic acid dihydrate ($C_2H_2O_4.2H_2O_2$), and ammonium metavanadate (NH_4VO_3) were all procured from SRL, India, and were of analytical grade, no further purification was done. Ethanol and double-distilled water (DW) were utilized as solvents throughout the entire synthesis process.

2.2 Preparation of Vanadium Pentoxide and Bi_2O_3 Doped V_2O_5

Each chemical had been used, without any additional purification. Vanadium was obtained from ammonium Meta vanadate (NH_4VO_3). The preparation of the vanadium pentoxide required dissolving 0.005 mol NH_4VO_3 in 50 mL of H_2O and C_2H_5OH solution, respectively. The pH value of the solution was adjusted to obtain 4 by using $H_2C_2O_4$ at a molar ratio of 1:3 ($NH_4VO_3/H_2C_2O_4$). After 30 minutes of stirring the mixture with a magnetic stirrer at ambient temperature, the material was transferred into a 50 mL Teflon-lined autoclave and kept at a temperature of 180 °C for a duration of 24 hours (Scheme 1). Bi_2O_3/V_2O_5 nanocomposite was produced utilizing the above mentioned process in three distinct percentages: 5%, 10%, and 15%. In the vanadium precursor solution, Bi^{3+} molar percentage, was altered from 5, 10, and 15%. To get a homogeneous solution, the mixture was magnetically stirred for one hour. To obtain Bi_2O_3/V_2O_5 nanocomposite, the solution was then placed within the Teflon liners, heated to 180°C for 24 hours, and then allowed to cool to ambient temperature, the obtained precipitates were repeatedly cleaned with deionized water and anhydrous alcohol before being dried for 10 hours at 60 °C [28].

2.3 Preparation of Electrodes for Supercapacitor Applications.

The electrochemical tests were carried out in a three-electrode configuration using an aqueous electrolyte of 2M KOH at ambient temperature. In order to fabricate the working electrode, Bi_2O_3/V_2O_5 nanocomposite were added to an N-methyl-2-pyrrolidone (NMP) solvent with carbon black and 10% polyvinylidene difluoride (PVDF) binder. It was well mixed and made a slurry [29]. After the homogenous slurry was made, it was applied to Ni-foil and dried for five hours at 80 ºC to eliminate the organic solvent. The electro-active material was approximately 4.5 mg cm^{-2}. In a three-electrode electrochemical cell, the platinum foil, material-coated Ni foil, and Ag/AgCl electrodes were utilized as counter, working, and reference electrodes respectively [30].

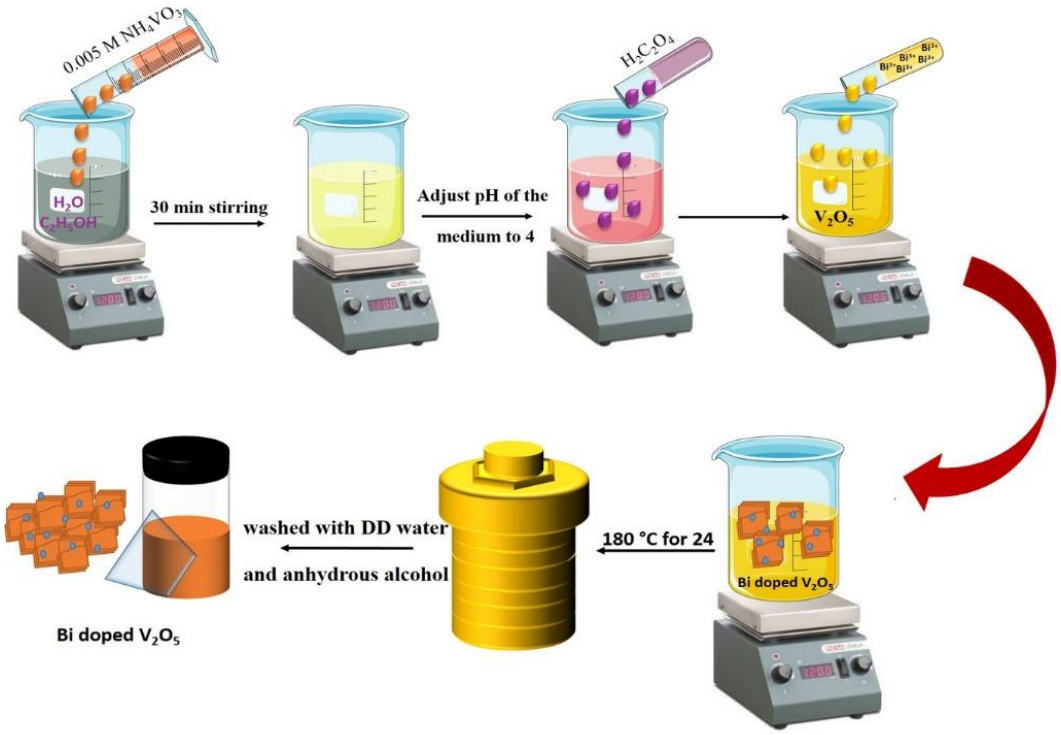

Scheme 1. Representation of preparation of Bi_2O_3/V_2O_5 nanocomposite.

2.4. Fabrication of asymmetric device

The asymmetric supercapacitor (ASC) device was constructed using prepared materials and activated carbon as the cathode and anode materials, respectively. The AC and PVDF binders were mixed in a 90:10 ratio to create the negative electrode. The NMP solvent was used to prepare the slurry, which was then applied to the Ni-foil current collector. In a hot air oven, the coated electrode was dried for 12 hours at 70 °C. Polytetrafluro-ethylene (PTFE) filter paper served as the separator, and PVA/KOH gel as the electrolyte. A 6 g of PVA and 3.58 g of KOH were blended with 60 mL of DI water to make the PVA/KOH electrolyte. The mixture was continuously stirred and heated to 90 °C to achieve homogeneity. All of the electrodes and the PTFE separator were soaked in PVA/KOH electrolyte before being sandwiched to form the ASC device. All electrochemical experiments were performed using the gel electrolyte, which was dried in an ASC apparatus. The characteristics of the supercapacitor were investigated using the electrochemical impedance spectroscopy (EIS), galvanostatic charge/discharge (GCD), and cyclic voltammetry (CV) methods. The specific capacitance value was assessed by Equation1.

$$C_{sp} = \frac{I \times \Delta t}{m \times \Delta V} \quad (1)$$

Where Cs, I, t, m, and V indicate the specific capacity, input current density (A g-1), discharge time (s), active material weight (mg), and potential window respectively [30].

2.5. Electrochemical characterization

The active materials, carbon black, and polyvinylidene fluoride (PVDF) were combined in an 8:1:1 weight ratio to create the 5%, 10%, and 15% Bi_2O_3/V_2O_5 electrodes. The mixed substances were ground with N-methyl-2-pyrrolidone (NMP) solvent and made into an electrolyte ink. The resultant electrolyte ink was coated onto the Ni-Foil, and then NMP was evaporated in a vacuum oven at 80 °C for 12 hours. The resultant final electrode holds 4.5 mg of active material. Platinum foil was utilized as the auxiliary electrode, while an Ag/AgCl electrode was employed as the reference electrode in a 2 M KOH electrolyte for three-electrode electrochemical measurements. The CHI660D electrochemical system was used to conduct two- and three-electrode electrochemical studies. Activated carbon was used as the negative electrode, 15% Bi_2O_3/V_2O_5 nanocomposite as the positive electrode, and PVA/KOH solution as the electrolyte in the assembly of an asymmetric capacitor (ASC) device. The PVA/KOH electrolyte was made by mixing 60 mL of DI water with 6 g of PVA and 3.58 g of KOH. To assure homogeneity, the mixture was constantly swirled as it was heated to 90 °C. The ASC device's separator was made of PTFE paper. To guarantee complete wetting and effective ionic interaction within the device, the separator, anode, and cathode were submerged in a PVA/KOH electrolyte prior to assembly. After that, all of the individual components are layered together to create the ASC device. The electrochemical characteristics were investigated using the resultant ASC device [30].

3. Results and Discussions

3.1 XRD Analysis

XRD is used to analyse the structural characteristics of synthesized pure V_2O_5 and Bi_2O_3/V_2O_5 nanocomposite. XRD data of the samples are presented in Figure 1(a, b). Figure 1(a) represents the XRD pattern for pure V_2O_5 displays characteristic peaks corresponding to an orthorhombic crystal, as we reported in our previous report [31]. Figure 1(b) represents the XRD of Bi_2O_3 incorporated V_2O_5. The peak positions well matched with the standard data for Bi_2O_3 with a monoclinic structure, with JCPDS Card No. 41-1449. The incorporation of Bi_2O_3 into V_2O_5 introduces new peaks at 2θ = 19.01, 28.94, 34.4, 40.02, 53.43, and 58.72, corresponding to (201), (101), (002), (110), (112), and (202). At low Bi (5%), the Bi_2O_3 reflections are minor, indicating most Bi is accommodated in the V_2O_5 host. At 10–15%, the peak intensity increases, evidencing partial phase segregation. Intensity of peaks increases as the percentage of Bi_2O_3 is increased from 5 to 15 %, indicating the incorporation of Bi_2O_3 into V_2O_5. It is observed that the phase was stable even when increasing the dopant concentration. The gradual peak broadening and slight peak shifting with increasing Bi concentration indicate reduced crystallite size, lattice distortion, and increased microstrain caused by Bi incorporation into the V_2O_5 lattice. The crystallite size was estimated from the diffraction peak using the Scherrer equation as shown in Table 1.

Table 1. Crystallite Size of the 5, 10 and 15 % Bi_2O_3/V_2O_5 samples

S. No	Sample	FWHM	Crystallite Size (nm)
1	5% Bi_2O_3/V_2O_5	0.176	46.35 nm
2	10% Bi_2O_3/V_2O_5	0.251	32.17 nm
3	15% Bi_2O_3/V_2O_5	0.261	30.96 nm

The crystallite size decreased from 46.35 nm for 5% Bi_2O_3/V_2O_5 to 30.96 nm for 15% Bi_2O_3/V_2O_5, confirming suppression of crystal growth and enhanced defect generation at higher Bi concentrations. XRD results suggest the emergence of minor Bi_2O_3-rich secondary phases at higher Bi concentrations, whereas XPS confirms strong Bi–O–V interfacial interaction and oxygen-vacancy-rich surface chemistry within the V_2O_5 matrix. The combined XRD and XPS analyses confirm that Bi incorporation induces lattice defects, oxygen vacancies, and mixed-valence states, which collectively contribute to improved electrochemical performance.

3.2. XPS analysis

Figure 2 (a-l) shows the XPS spectra of Bi_2O_3/V_2O_5 at 5, 10, and 15% confirming the presence of V, O, Bi, and C elements, demonstrating successful incorporation of Bi into the V_2O_5 lattice. Survey spectrum of pure V_2O_5 is reported in our previous article [31]. The high-resolution V 2p spectra reveal the characteristic doublets of V^{5+} with V $2p_{3/2}$ located at 516.98 eV and V $2p_{1/2}$ at 524.42 eV for 5% Bi, corresponding to a spin–orbit splitting of 7.44 eV. At 10%, the V $2p_{3/2}$ and V $2p_{1/2}$ peaks shift slightly to 517.15 eV and 524.74 eV, respectively, with an increased splitting of 7.59 eV, indicating lattice perturbation due to Bi incorporation. For 15% Bi, the V2p peaks are observed at 516.90 eV and 524.41 eV, with a splitting of 7.51 eV. Across the series, subtle broadening and the emergence of shoulders in the V2p region signify the partial reduction of V^{5+} to V^{4+}, which becomes more pronounced at higher Bi_2O_3 incorporation. [32, 33] This evolution suggests improved electronic conductivity arising from mixed valence states of vanadium. The O1s spectra further corroborate these observations. At 5% Bi, the lattice oxygen (O^{2-}) peak appears at 529.74 eV [34]. At 10% Bi the lattice oxygen peak shifts to 529.96 eV, while the defect oxygen component grows stronger, implying an increase in oxygen vacancies. Similarly, at 15% Bi the lattice oxygen is observed at 529.89 eV with the highest contribution from surface and defect oxygen, confirming a progressive rise in oxygen-vacancy density with Bi content [35]. These vacancies are expected to facilitate ionic transport and contribute to enhanced redox activity. The Bi 4f spectra display well-defined doublets at 159.28 eV, 159.52 eV, 159.03 eV (Bi $4f_{7/2}$) and 164.60 eV, 164.97 eV, 164.35 eV (Bi $4f_{5/2}$), with spin–orbit splitting values 5.32 eV, 5.45 eV and 5.28 eV for 5, 10, and 15% nanocomposite, which is consistent with Bi^{3+} in an oxide environment. The composite with the Bi 4f component from the V_2O_5 matrix is also evidenced by the increase in the intensity and the broadening of the Bi 4f peaks upon Bi concentration. No phase segregation is observed [36, 37]. Furthermore the substitution of Bi^{3+} in V_2O_5 leads to the formation of oxygen vacancies and a partial reduction of V^{5+} to V^{4+} resulting in an electron-rich and defect-engineered lattice as revealed by the XPS analysis. At 5%, the structure is close to stoichiometric V_2O_5 with only a few oxygen vacancies and at 10% the lattice is significantly disturbed with an increase in defect oxygen and mixed valence behaviour [38]. At 15% the concentration of oxygen vacancies and the contribution of V^{4+} reaching their maximum thus resulting in the highest density of redox-active sites. These changes will facilitate the electron transfer and the electrochemical performance will be improved at high Bi concentrations.

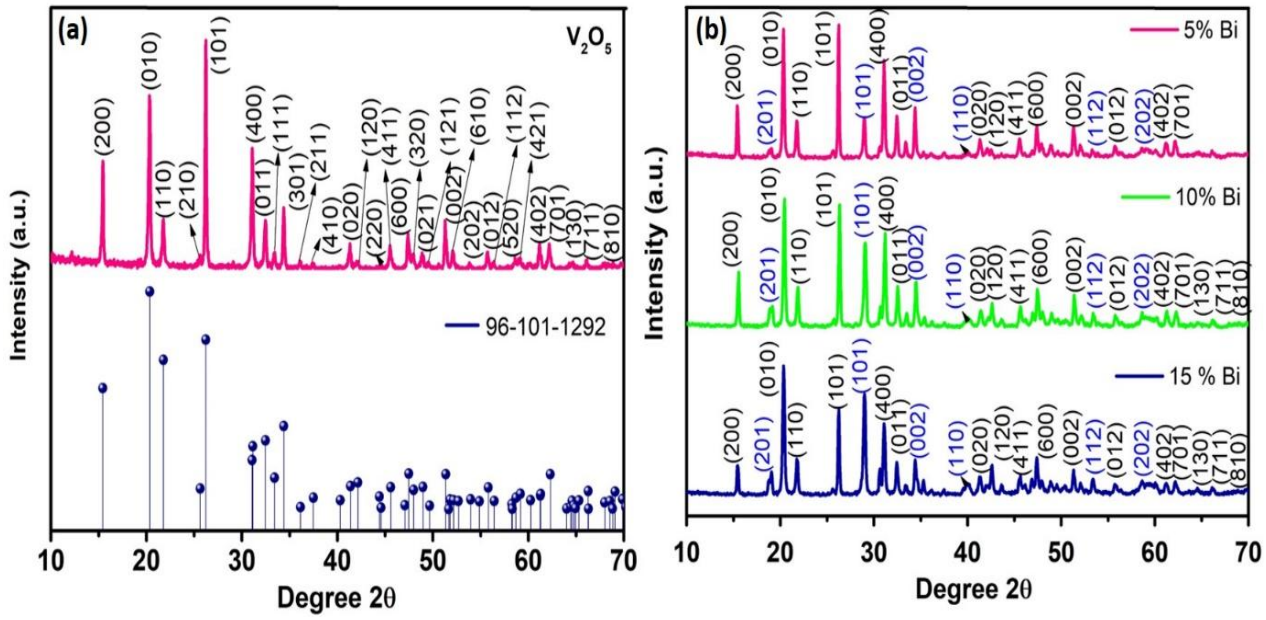

Figure 1. XRD spectrum of **(a)** V_2O_5 and **(b)** 5, 10 and 15% Bi_2O_3 /V_2O_5 nanocomposite.

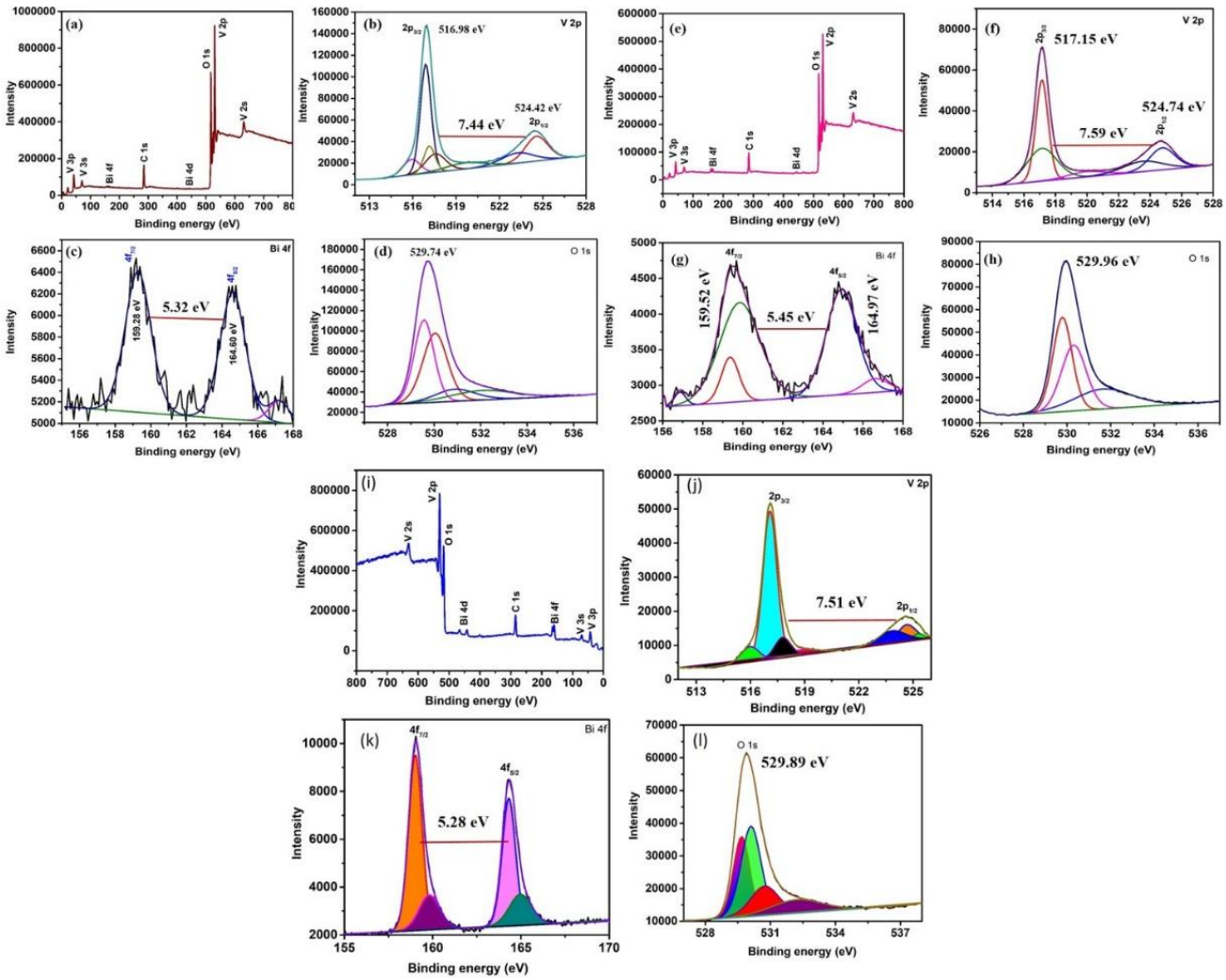

Figure 2. **(a, e, i).** XPS survey spectrum 5, 10 and 15% of Bi_2O_3/V_2O_5 **(b, f, j)** Core spectrum of V 2p, **(c, g, k)** Core spectrum of Bi 4f, and **(d, h, l)** Core spectrum of O 1s.

3.3 FT-IR analysis of Bi_2O_3/V_2O_5 nanocomposite

FT-IR spectra for V_2O_5 with different concentrations of bismuth oxide (5%, 10%, and 15%) are shown in Figure. 3(a-c). The figures confirm that the V_2O_5 lattice is present after the Bi as all the samples have vibrational bands characteristic of orthorhombic V_2O_5, especially in the fingerprint region (400–1200 cm^{-1}). The Bi content increases a significant decrease in the overall transmittance. This is indicative of enhanced light absorption as a result of a higher composite loading. Increased structural disorder and the existence of localized defect states can be used to explain this phenomenon. The bands formed at 1013, 1014, and 1023 cm^{-1} are the vibrational modes of the V=O and V–O–V bonds that were stretched, respectively. The bands at 827, 823, and 832 cm^{-1} signal the creation of the Bi-O-Bi bond, thus the integration of Bi into the V_2O_5 lattice is confirmed. These peaks demonstrate broadening and minor changes with high Bi concentrations, which could mean that the lattice is distorted and that Bi ions are substituted or interstitially incorporated in the V_2O_5 matrix. Besides that, weak bands or changes in intensity in the mid-infrared region close to 1600–3500 cm^{-1} can be assigned to surface hydroxyl groups and adsorbed water molecules coming from the dopant-induced changes in surface morphology and porosity. To sum up, spectral changes upon Bi at higher levels confirm not only the incorporation of bismuth into the V_2O_5 structure but also reflect changes in the local bonding environment which may have direct implications for the material's optical and electrochemical properties.

3.4 Raman Analysis

The Raman spectra of V_2O_5 with 5%, 10%, and 15% Bi_2O_3 as shown in Figure. 4 exhibit changes in the intensity and position of the peaks that indicate the structural and vibrational changes of the V_2O_5 lattice due to the Bi_2O_3 addition. Pure V_2O_5 is known to have very clear Raman features, especially around 118, 148, 233, 290, 410, 548, 668, and 700 cm^{-1}, that can be assigned to the bending and stretching vibrations of V–O–V and V=O bonds. These vibrations serve as a reference for the doped samples.

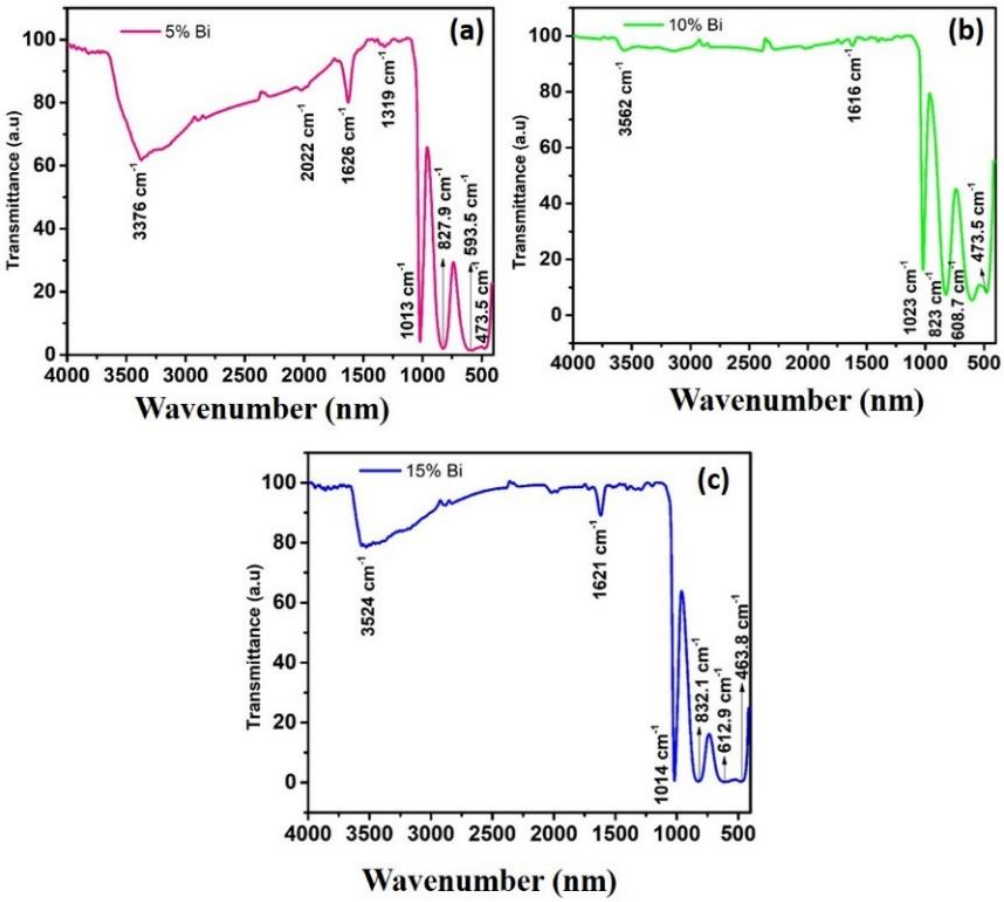

Figure 3. (a-c). FT-IR spectrum of 5, 10, and 15% Bi_2O_3/V_2O_5 nanoparticle.

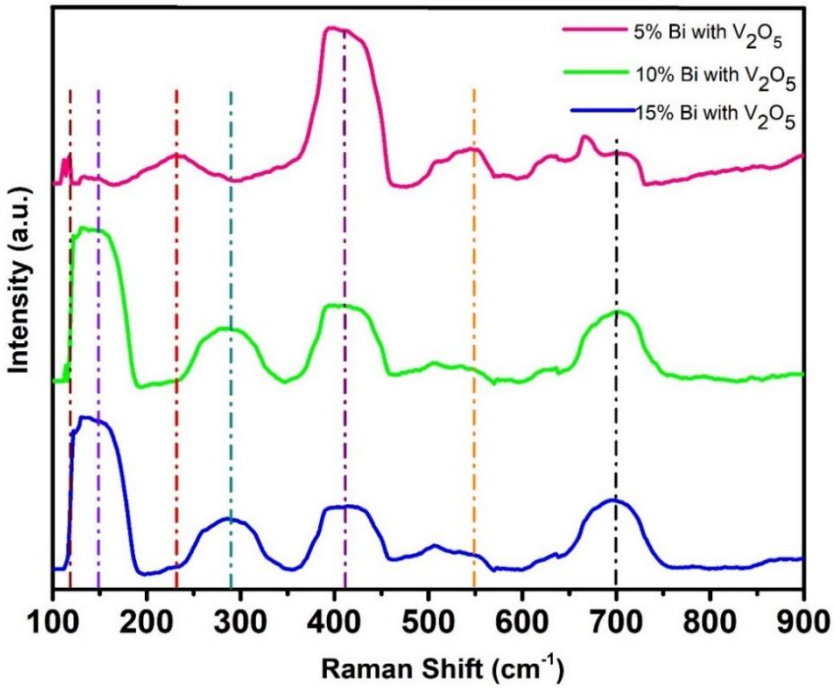

Figure 4. Raman spectrum of 5, 10, and 15% Bi_2O_3/V_2O_5 nanocomposite.

The low-frequency modes at 118 and 233 cm^{-1} were associated with the Bi_2O_3/V_2O_5 lattice vibrations due to the movements of the translation and rotation of the structural units [39]. The peaks at 233 and 410 cm−1 are assigned to V=O, and the shoulder peaks at 548 and 668 cm−1 are related to Bi-O and Bi- O-Bi bonds, respectively [40]. The asymmetric stretching of the V–O bond contributed to the shoulder peak at 700 cm^{-1} [41].

3.5 Optical property

The optical absorbance and band gap characteristics of V_2O_5 tailored with various bismuth oxide concentrations were thoroughly explored by means of UV-Vis diffuse reflectance spectroscopy (DRS). The absorbance spectra shown in Figure. 5(a) reveal that the absorption characteristics vary significantly as the Bi_2O_3 concentration changes from 5% to 15%. The 5% Bi_2O_3 sample exhibits higher absorbance across the visible spectrum, which is indicative of a strong light harvesting capability. Contrary to this, the 10% and 15% Bi_2O_3 concentrations show a drastic decrease in absorbance, which suggests that the excessive Bi_2O_3 incorporation might lead to changes in the structure or electronic properties that lower the optical density. The Tauc plots from Figure. 5(b-d) depict an indirect yet uniform tendency of the optical band gap energy with the increase in Bi_2O_3 content.

The band gap for the Bi_2O_3 5% modified V_2O_5 is found to be 2.13 eV. In the 10% Bi_2O_3 sample, the band gap is slightly larger, about 2.14 eV. The maximum band gap value of 2.17 eV is attributed to the 15% Bi_2O_3 sample [42]. The slow increase of the band gap with an increase of Bismuth oxide content can be related to the replacement of Bismuth that changes the local electronic structure of V_2O_5 through lattice distortion. Where there is only a small amount of Bismuth oxide, Bismuth acts as a donor and only slightly changes the electronic transitions. On the other hand, at high Bismuth levels, a blue shift can take place leading to the Fermi level entering the conduction band causing a significant increase in the optical band gap [43].

3.6 Morphological Analysis

The morphology and elemental composition of the Bi_2O_3/V_2O_5 nanocomposites that were synthesized with different proportions of Bi_2O_3 (5, 10, and 15 wt%) were extensively characterized by field emission scanning electron microscopy (FE-SEM) along with energy-dispersive X-ray spectroscopy (EDX). The obtained images Figure.6 (a-h) distinctly show the alterations of morphology and successful compositional tuning resulting from Bi_2O_3 into the V_2O_5 matrix. V_2O_5 sample exhibits a disordered morphology comprised of aggregated microstructures with flake-like and plate-like features being the main constituents.

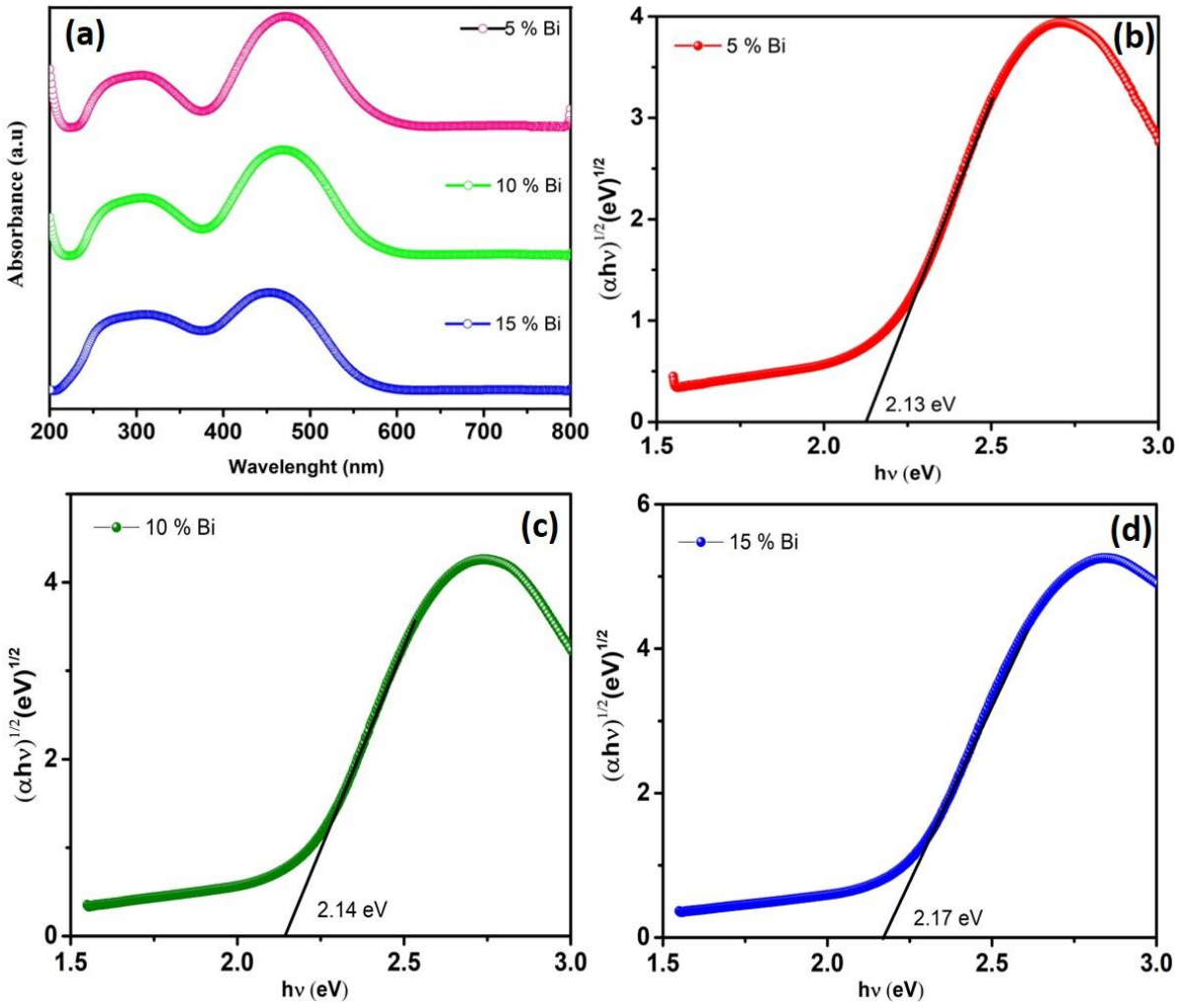

Figure 5 (a) DRS UV and **(b-d)** Band gap of 5, 10, and 15% Bi_2O_3/V_2O_5 nanoparticle.

The particles are oriented in a random manner and are packed loosely, thus forming a porous network with quite large interparticle voids. The surface is rough and uneven which is indicative of uncontrolled crystal growth and poor connectivity between grains. Such a morphology is representative of Bi_2O_3 obtained by conventional methods, where nucleation dominates over directional growth, leading to a non-uniform particle distribution. On introducing 5 wt% Bi_2O_3 Figure 6 (a, b), the morphology change is very significant. The structure lies in the layered configuration which is made up of stacked nanosheets that are more ordered and compact in their arrangement. These nanosheets appear to grow preferentially along crystallographic directions, which is a likely indication that Bi_2O_3 acts as a structure-directing agent. The better ordering and lower void spaces when compared with pure V_2O_5 are indicative of enhanced crystallinity and structural stability. Higher Bi_2O_3 up to 10, 15 wt% Figure 6 (d, e, g, h) leads to a very complicated hierarchical morphology. The microstructure consists of joined nanosheets, co-existence of nanosheets alongside nanoparticles implies strong local interfacial interactions between Bi_2O_3 and V_2O_5 phases that facilitate charge transfer and surface reactions, which are the requirements for an effective and productive system. The elemental composition and chemical purity of the samples were also confirmed by EDX analysis Figure 6 (c, f, i). The spectra of all samples show sharp peaks that belong to bismuth (Bi), vanadium (V), and oxygen (O), confirming the synthesis of Bi_2O_3/V_2O_5 nanocomposites. Besides the elemental peaks of the bismuth vanadate composites, no other impurity peaks were observed indicating a high level of purity in the synthesized materials. The EDX spectra confirm the Bi_2O_3 (5, 10, and 15 wt%) into the V_2O_5 matrix. Characteristically, 5 wt% Bi_2O_3 sample was dominated by V (~49.2 wt %) and O (~45.2 wt %) with a minor amount of Bi (~5.6 wt %) which implied that the Bi particles are well dispersed. At 10 wt%, the Bi content increases (~9.8 wt %) while the V content decreases (~39.4 wt %) which reflects an increased interaction of Bi_2O_3 with V_2O_5. For the 15 wt% specimen, the Bi level was further raised (~11.4 wt %) which is a clear indication of a higher loading of Bi while maintaining the V_2O_5 structure. The absence of impurity peaks at each stage confirmed that the sample was pure, and the pattern of changing composition indicated the effective formation of hetero structures as the Bi_2O_3 content increased. Combined FE-SEM and EDX studies clearly show that Bi_2O_3 plays a major role in shaping both the physical form and chemical makeup of V_2O_5-based composites.

Then, to examine the spatial distribution of elements more thoroughly, EDS elemental mapping was performed, and the results are presented in Figure 7 (mapping images). The overlay images and Bi maps effectively reveal the distribution pattern of Bi_2O_3 inside the V_2O_5 matrix. For the 5 wt% composite, Bi is uniformly distributed at low intensity, indicating a very fine distribution without significant agglomeration. Only a few small bright spots show slight clustering; however, the sample remains generally homogeneous overall. For 10 wt% Bi_2O_3, the Bi signal gets stronger and more evenly distributed throughout the matrix, demonstrating better uniformity and a stronger Bi_2O_3/V_2O_5 interaction. This uniform dispersion is also reflected in the hierarchical morphology that was observed and it further implies an ideal compositional balance. Bi mapping for the 15 wt% sample identifies high-intensity localized areas, showing that there are still some agglomerated Bi_2O_3 particles.

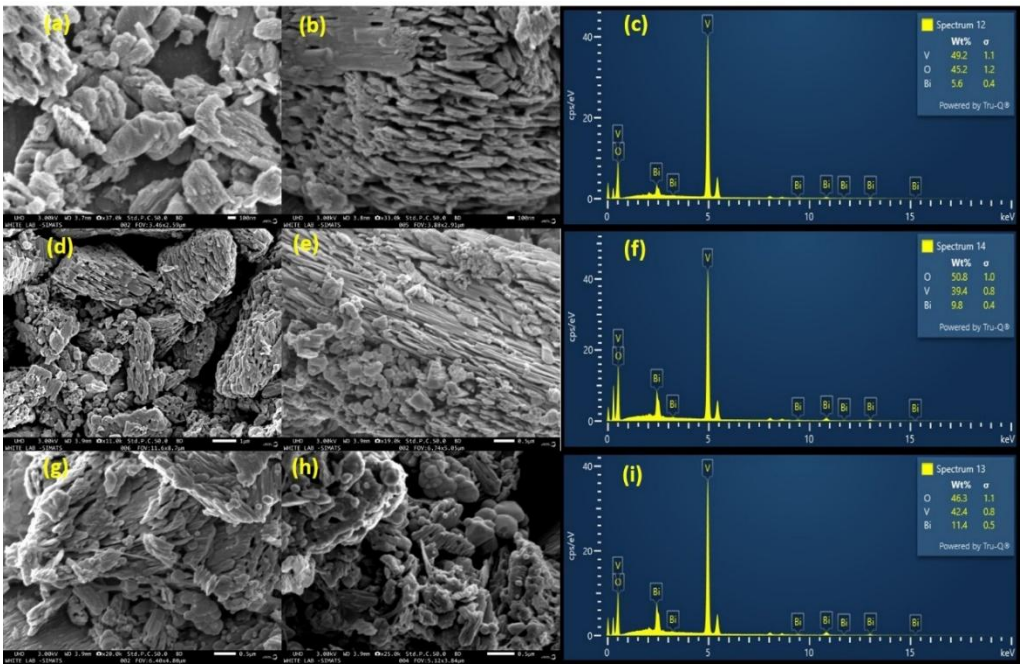

Figure 6. FE-SEM images and EDX of **a)** 5% Bi_2O_3/V_2O_5, **b)** 10% Bi_2O_3/V_2O_5 and **c)** 15% Bi_2O_3/V_2O_5 Nanocomposite.

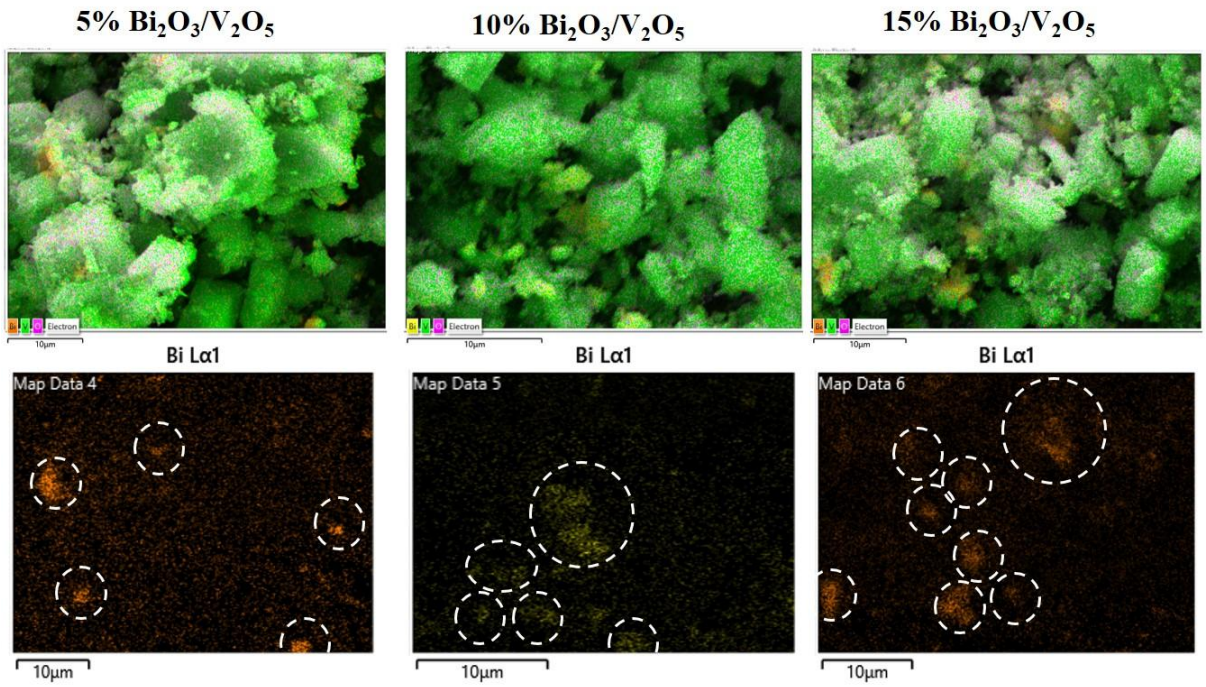

Figure 7. Elemental Mapping of **a)** 5% Bi_2O_3/V_2O_5, **b)** 10% Bi_2O_3/V_2O_5 and **c)** 15% Bi_2O_3/V_2O_5.

Although Bi still spreads across the area, the existence of large clusters points to lower uniformity at higher loading. Overall, mapping results confirm a change from uniform dispersion (5 wt%) to best homogeneous distribution (10 wt%) and partial agglomeration (15 wt%), which is in agreement with FE-SEM observations.

4. Electrochemical Analysis

The electrochemical properties of the 5% Bi_2O_3/V_2O_5, 10% Bi_2O_3/V_2O_5 and 15% Bi_2O_3/V_2O_5 electrodes were demonstrated using 2 M KOH electrolyte in three three-electrode electrochemical cell. The cyclic voltametric (CV), galvanostatic charge/discharge (GCD) and Electrochemical Impedance (EIS) techniques were utilized to evaluate electrochemical properties. The electrochemical response of all electrodes was investigated using CV measurements at various sweep rates, extending from 5 to 100 mV s^{-1}, as shown in Figure 8 (a-c).

The Faradaic processes in all CV curves are indicated by the appearance of prominent redox peaks, signifying that Faradaic redox reactions are the primary energy storage process in 5% Bi_2O_3/V_2O_5, 10% Bi_2O_3/V_2O_5 and 15% Bi_2O_3/V_2O_5 electrodes [44]. The redox reactions of V_2O_5 material include the V5+/V4+ and V4+/V3+ redox transitions, which occur in the bulk of the material in the 2 M KOH electrolyte as well as on its surface. [45, 46] The following chemical equation (1) illustrates the reactions that define the redox processes.

$$V_2O_5 + xK^+ + xe^- \rightleftarrows K_xV_2O_5(x - mole\ fraction\ of\ K + ions) \quad (1)$$

Interestingly, Bi improves the conductivity of the electrodes during the electrochemical process without going through any redox reactions. The high ionic conductivity associated with Bi arises from its inherent defect structure and high polarizability [47]. These characteristics facilitate efficient charge transport, improving overall electrochemical performance. This is confirmed by the area under the CV curves. The 15% Bi_2O_3/V_2O_5 electrode exhibits a significantly larger area compared to the 5% Bi_2O_3/V_2O_5 electrode, clearly indicating that the higher Bi level in the 15% Bi_2O_3/V_2O_5 electrode enhances its electrochemical activity.

Furthermore, the high area under the CV curves demonstrates the high supercapacitor properties of the 15% Bi_2O_3/V_2O_5 electrode material. [48] Additionally, the exceptional reversibility of electrodes is designated by the symmetrical nature of the anodic and cathodic peaks. Furthermore, as scan rates rise from 5 to 10 mV s−1, the CV curve does not alter, suggesting enhanced mass transport, superior electron transfer within the electrode materials, and low equivalent series resistance. The internal resistance of the active electrode material is mostly responsible for the positive shift in the oxidation peak potential and the negative shift in the reduction peak potential with increasing sweep rates. [49] Similar CV curves and quasi-symmetric redox peaks are detected as the scan rates raises, indicating the optimal pseudocapacitance properties and high-rate capabilities of electrode materials [50].

To further explore capacitive characteristics, GCD tests were conducted for all electrodes with a potential limit of 0 to 0.6 V with 1 to 20 A g^{-1} of current density values, as shown in Figure. 8(d-f).

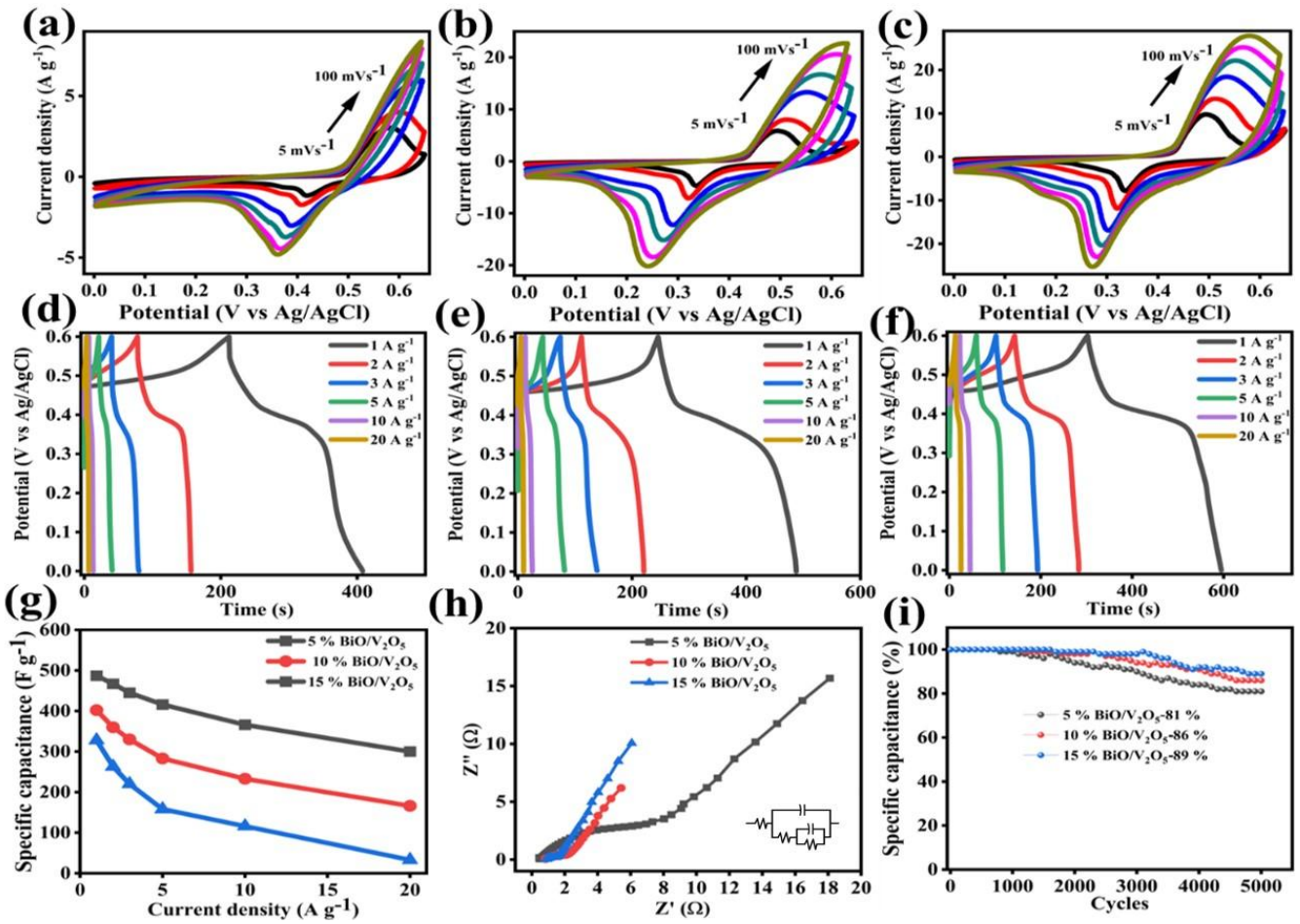

Figure 8. CV analysis of **(a)** 5 % Bi_2O_3/V_2O_5, **(b)** 10 % Bi_2O_3/V_2O_5, and **(c)** 15 % Bi_2O_3/V_2O_5, electrodes. GCD analysis of **(d)** 5 % Bi_2O_3/V_2O_5, **(e)** 10 % Bi_2O_3/V_2O_5, and **(f)** 15 % Bi_2O_3/V_2O_5, electrodes. **(g)** Rate capability, **(h)** EIS and **(i)** cyclic stability of all electrodes.

Table 2. An analysis of the performance of the supercapacitor in comparison to the previously reported articles.

S.No	**Material**	**Electrolyte**	**Current Density / Scan Rate**	**Voltage Window**	**Cycling Stability**	**Performance**	**Ref.**
1	V_2O_5 nanoporous network	0.5 M K_2SO_4	0.1 A g^{-1}	0–1.0 V	82% after 3000 cycles	316 F g^{-1} at 100 mA g^{-1}	[51]
2	Porous V_2O_5 nanorods/rGO	5 M $LiNO_3$	0.5 A g^{-1}	0–1.0 V	85% after 5000 cycles	450.5 F g^{-1} at 0.5 A g^{-1}	[52]
3	TiO_2-V_2O_5	Hydroquinone mixed with 1 M KCl	2 mV s^{-1}	0–0.8 V	Not reported	310 F g^{-1} at 2 mV s^{-1}	[53]
4	RGO/V_2O_5	1 M Na_2SO_4	10 mV s^{-1}	0–1.0 V	80% after 2000 cycles	218.4 F g^{-1} at 10 mV s^{-1}	[54]
5	V_2O_5 nanowires	1 M $LiNO_3$	2 A g^{-1}	0–0.6 V	84% after 5000 cycles	351 F g^{-1} at 2 A g^{-1}	[45]
6	V_2O_5 nano crystals	6 M KOH	0.5 A g^{-1}	0–1.0 V	87% after 5000 cycles	310 F g^{-1} at 1 A g^{-1}	[55]
7	Carbon-coated V_2O_5	0.5 M K_2SO_4	1 A g^{-1}	0–0.6 V	88% after 5000 cycles	417 F g^{-1} at 0.5 Ag^{-1}	[56]
8	15% Bi_2O_3/V_2O_5	2 M KOH	1 A g^{-1}	0–0.6 V	89% after 5000 cycles	487 F g^{-1} at 1 A g^{-1}	Present work

Table 3 Equivalent circuit fitting parameters obtained from EIS analysis of 5%, 10%, and 15% Bi_2O_3/V_2O_5 electrodes.

Sample	5% Bi_2O_3/V_2O_5	10% Bi_2O_3/V_2O_5	15% Bi_2O_3/V_2O_5
$CPEc_1$ (μS. s^n) cm^{-2}	2.12	5.84	4.18
n_{c1}	0.84	0.78	0.81
R_c (ohm cm^2)	3.19	0.84	1.97
CPE_{c2} (μS. s^n) cm^{-2}	1.89	3.51	2.84
n_{c2}	0.76	0.76	0.8
R_{ct} (kohm cm^2)	7.18	1.37	3.2

The fact that all the GCD curves are nonlinear characteristics and that the corresponding voltage plateaus closely match the CV curves Figure 6(a-c) further demonstrates the pseudocapacitive property of the electrode material. Furthermore, the absence of distinctive electric double-layer capacitance (EDLC) behaviour, characterized by a nearly triangular GCD profile, designates that the charge storage mechanism of the electrode materials is principally controlled by faradaic redox processes.

The outstanding conductivity property of the 15% Bi_2O_3/V_2O_5 electrode is signified by the insignificant voltage (IR) drop in the discharge curves, which is lower than that of 5% Bi_2O_3/V_2O_5 and 10% Bi_2O_3/V_2O_5 electrodes. The outstanding conductivity of the 15% Bi_2O_3/V_2O_5 electrode is further confirmed by the negligible voltage (IR) drop in the discharge curves, which is lower than those of the 5% Bi_2O_3/V_2O_5 and 10% Bi_2O_3/V_2O_5 electrodes [57]. The specific capacitance and specific capacity values were calculated using Equations (2) and (3), respectively.

$$Specific\ capacitance = \frac{I \times \Delta t}{m \times \Delta V} \quad (F\ g^{-1}) \qquad (2)$$

$$Specific\ capacity = \frac{I \times \Delta t}{m} \quad (C\ g^{-1}) \qquad (3)$$

Where I (A) denotes current density, m refers to electrode active material weight (mg), t corresponds to discharge time (s), and V denotes voltage window (V), respectively. Impressively, the 5% Bi_2O_3/V_2O_5, 10% Bi_2O_3/V_2O_5 and 15% Bi_2O_3/V_2O_5 electrodes offer the specific capacitance values of 328, 402 and 487 F g^{-1}, whereas the specific capacity values of 197, 241, and 292 C g^{-1}, respectively, at 1 A g^{-1} of current density. At 20 A g^{-1}, the 15% Bi_2O_3/V_2O_5 electrode sustains 61% of its capacitance, which is higher than 5% Bi_2O_3/V_2O_5 (41%) and 10% Bi_2O_3/V_2O_5 (13%) electrodes, as shown in Figure 8(g). The EIS spectra Figure 8(h) of all electrodes show the ohmic resistance and interface or charge transfer resistance components. The 15% Bi_2O_3/V_2O_5 electrode provides lower Rs (0.69 Ω) and Rct (1.7 Ω) values when compared to 5% Bi_2O_3/V_2O_5 (Rs = 0.85 Ω and Rct = 2.2 Ω) and 10% Bi_2O_3/V_2O_5 (Rs = 0.33 Ω and Rct = 8.1 Ω) electrodes.

The electrochemical impedance spectroscopy (EIS) analysis of the 5%, 10%, and 15% Bi_2O_3/V_2O_5 electrodes was carried out using an equivalent circuit model consisting of solution resistance (R_s), charge transfer resistance (Rct), and two constant phase elements (CPE_1 and CPE_2). Among the studied samples, the 15% Bi_2O_3/V_2O_5 electrode exhibited superior electrochemical performance due to its balanced resistance and enhanced capacitive behaviour. The electrode showed low solution resistance (R_s = 1.97 Ω cm^2), indicating efficient ion transport and good electrical conductivity as shown in Table 3. The higher CPE values and n values closer to unity confirmed improved pseudocapacitive behaviour, enhanced charge storage capability, and better interfacial homogeneity. In addition, the moderate charge transfer resistance (Rct=3.2kΩ cm^2) suggested effective electron transport kinetics and stable electrochemical reactions. The enhanced performance is attributed to the synergistic interaction between Bi_2O_3 and V_2O_5, which improves electrolyte diffusion, electroactive sites, and conductivity. Overall, the 15% Bi_2O_3/V_2O_5 electrode demonstrated improved electrochemical stability and promising potential for advanced supercapacitor applications.

The cyclic stability of all electrodes was assessed using 5000 GCD cycles at 10 A g^{-1}, as shown in Figure 8(i). After 5000 GCD cycles, the 5% Bi_2O_3/V_2O_5, 10% Bi_2O_3/V_2O_5 and 15% Bi_2O_3/V_2O_5 electrodes retain 81 %, 86 %, and 89% of their initial specific capacitance, further representing the distinctive electrochemical stability feature of the 15% Bi_2O_3/V_2O_5 electrode. Among all the electrodes 15% Bi_2O_3/V_2O_5 electrode provides the high specific capacitance, rate capability and long cyclic stability owing to the following factors: (i) the incorporation of Bi induces a more open and defective crystal structure, which enables easier ion penetration and diffusion. This enhances the ion-accessible active surface area and contributes to higher specific capacitance and rate capability properties. (ii) The formation of nanoparticles and nanorods offers a large electroactive surface area property, rapid diffusion paths for ions and electrons, and enhanced contact with the electrolyte. This morphology promotes better charge storage, faster kinetics, and high utilization of active materials. (iii) High Bi concentration helps in maintaining structural integrity by preventing volume expansion or collapse during repeated GCD cycles. This pays off in the long-term cycling stability. Additionally, a two-electrode asymmetric device was fabricated using AC

and 15% Bi_2O_3/V_2O_5 electrodes with a PVA/KOH electrolyte and PTFE separator. The properties of the Bi_2O_3/V_2O_5//AC ASC device were assessed utilizing CV, GCD, and EIS testing. A charge balance between the anode and cathode was attained by altering the mass of electroactive materials (Equations (4) and (5)).

$$q^+ = q^- \quad (4)$$

$$\frac{m_+}{m_-} = \frac{C_- \times \Delta V_-}{C_+ \times \Delta V_+} \quad (5)$$

Where (+) and (-) indicate cathode and anode, respectively. Where Q, m, C, and V denote charges, mass of electrode material, specific capacitance, and voltage limit, respectively. The charge-storage mechanism was analyzed using scan-rate-dependent CV measurements to distinguish surface-controlled and diffusion-controlled contributions. The relationship between peak current (i) and scan rate (v) was analyzed using the power-law equation:

$$i = av^b \quad (6)$$

where the obtained b-values for the 15% Bi_2O_3/V_2O_5 electrode were close to 0.82, indicating predominantly pseudocapacitive behavior with combined surface-controlled and diffusion-assisted charge storage. Further quantitative separation of capacitive and diffusion contributions was performed using Dunn's equation:

$$i(V) = k_1 v + K_2 v^{\frac{1}{2}} \quad (7)$$

The analysis revealed that the capacitive contribution increased with scan rate, confirming enhanced surface-controlled charge storage and rapid electrochemical kinetics for the 15% Bi_2O_3/V_2O_5 electrode. The coulombic efficiency was calculated using:

$$\eta = (Q_{discharge}/Q_{charge}) \times 100 \quad (8)$$

where $Q_{discharge}$ and Q_{charge} represent discharge and charge times, respectively. The 15% Bi_2O_3/V_2O_5 electrode exhibited a columbic efficiency of approximately 96%, indicating excellent reversibility and stable charge-storage behavior. In addition, replicate electrochemical measurements were carried out, and the average capacitance retention after 5000 cycles was determined to be 89 ± 1.8%, confirming good reproducibility and cycling stability. The CV analysis for the positive and negative electrode material in 2 M KOH aqueous electrolyte at the scan rate of 50 mV s^{-1} is shown in Figure 9(a), which suggests that 15% Bi_2O_3/V_2O_5 and AC are appropriate for utilization as anode and cathode, respectively. The potential window for the 15% Bi_2O_3/V_2O_5 electrode is between 0 and 0.65 V, and for the AC electrode displaying EDLC behaviour, it is between -1.2 and 0 V. As seen in Figure 9(b), a CV test was performed at 50 mV s^{-1} throughout a range of voltage windows from 0.8 V to 1.8 V to verify the device's appropriate operating voltage window. When the cell voltage is increased to .6 V, polarization phenomena are observed, suggesting that 0–1.6 V is an appropriate voltage window. The CV analyses of the ASC are shown in Figure. 9(c), which was acquired at a cell voltage of 1.6 V over a range of scan speeds from 5 to 100 mV s^{-1}. The CV curves preserve their initial shape property as the scan rate increases, demonstrating the superior reversible energy storage and increased electron transport property of the Bi_2O_3/V_2O_5//AC device. Different current densities (1 Ag^{-1} to 20 Ag^{-1}) are used to measure the GCD analysis of the ASC device, and the corresponding graph is displayed in Figure 9(d). The Bi_2O_3/V_2O_5//AC ASC device provides the specific capacitance of 108 F g^{-1} (173 C g^{-1}) at 1 A g^{-1}. The specific capacitance of the electrode material shows a gradual decline as the scan rate raises Figure 9(e).

This behaviour can be attributed to the time-limited nature of ion diffusion and charge storage mechanisms. Both EDLC and faradaic processes facilitate effective charge accumulation at a lower sweep rate since the electrolyte ions have sufficient time to infiltrate the internal pores and interact with the electrode's whole active surface area. Though as the scan rate rises, the available time for ion diffusion and redox reactions becomes limited. Consequently, only the outer region of the electrode material is effectively employed, while the inner active sites remain underutilized. This reduced ion accessibility at higher scan rates results in a lower overall charge storage, thereby decreasing the measured specific capacitance [58] The energy and power density values in Figure 9(f) are calculated using equations (9) and (10):

$$E_{cell} = \frac{1}{2\times3.6} \times C_{sp} \times \Delta V^2 \quad (9)$$

$$P_{cell} = \frac{3600 \times E_{cell}}{\Delta t} \quad (10)$$

where C_{sp}, ΔV, and Δt signify the specific capacitance values, device voltage, and discharging time, respectively. The assembled 15% Bi_2O_3/V_2O_5//AC asymmetric supercapacitor device delivered a maximum energy density of 38.4 Wh kg^{-1} at a power density of 800 W kg^{-1} at 1 A g^{-1}. At a higher current density of 20 A g^{-1}, the device retained a power density of 16,000 W kg^{-1} with a corresponding energy density of 4.4 Wh kg^{-1}. The attained energy and power density values are superior to previous published works, such as V_2O_5/vertically-aligned carbon nanotubes (32.3 Wh kg^{-1} and 118 W kg^{-1}) [59] $V_2O_5 \cdot 0.6H_2O$ nanoribbons (29 Wh kg^{-1} and 2 kW kg^{-1})[60], Fe_2O_3 and V_2O_5 nanofibers (32.2 W h kg^{-1} and 128.7 W kg^{-1}) [61], V_2O_5/h-boron nitride (25 Wh kg^{-1} and 2373 W kg^{-1}) [46], vanadium oxides nanosheets (4.7 Wh kg^{-1} and 7.992 kW kg^{-1}) [62], and V_2O_5 nanorods/reduced graphene oxide composite (33.5 W h kg^{-1} and 425.6 W kg^{-1}).

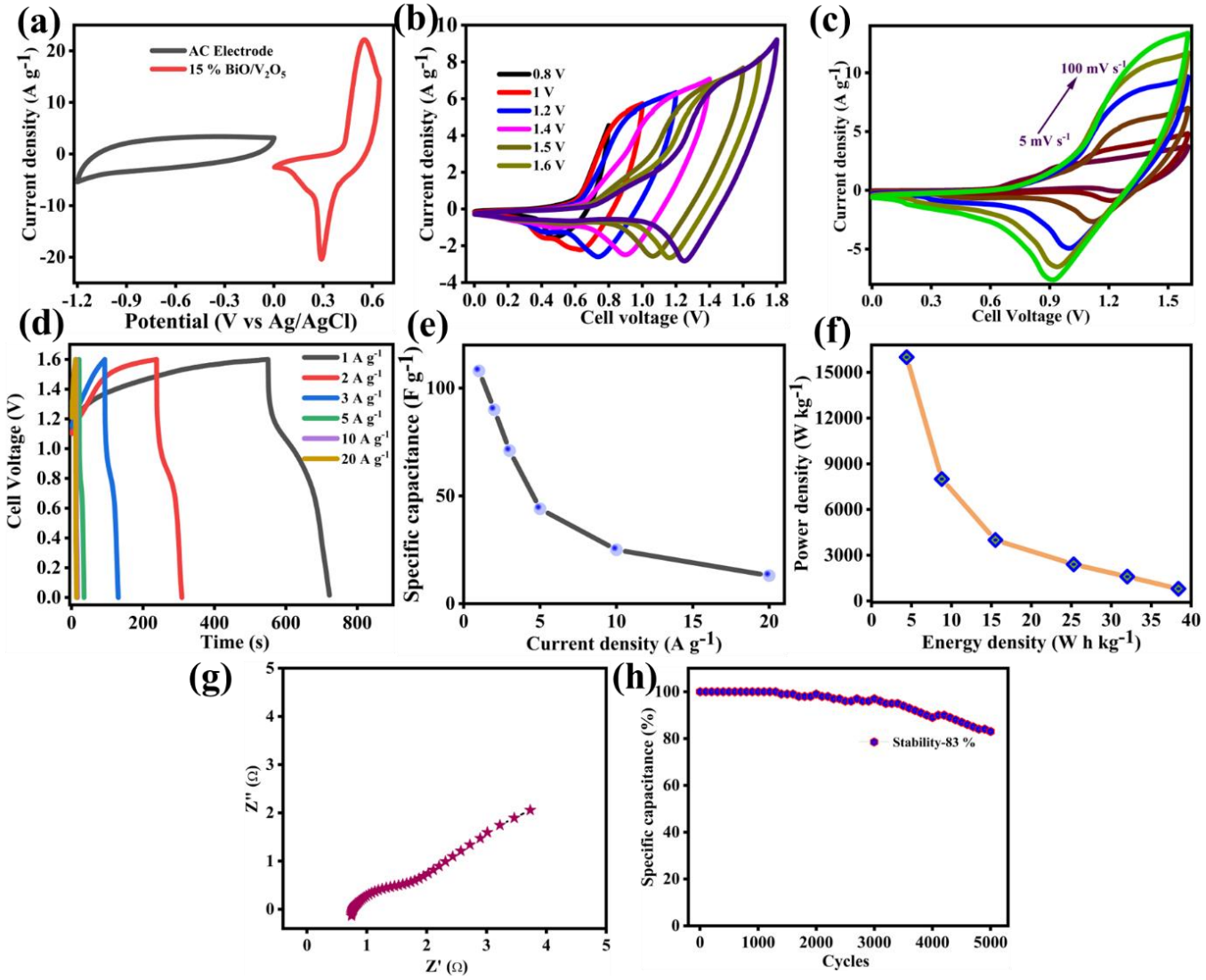

Figure 9. Device analysis. **(a)** CV curves anode and cathode at 50 mV s^{-1}, **(b)** CV analysis with different cell voltages, **(c)** CV analysis, **(d)** GCD analysis, **(e)** Specific capacitance vs Current density, **(f)** Ragone plot **(g)** EIS, and **(h)** cyclic stability analysis.

The results of the EIS test Figure. 9(g) showed low resistance qualities with Rs and Rct values of 0.73 Ω and 1.83 Ω, respectively. The cycle stability of Bi_2O_3/V_2O_5//AC device is further assessed via repeated 5000 GCD cycles at a fixed current density of 10 A g^{-1}, as illustrated in Figure. 9(h). After 5000 continuous charge-discharge cycles, the electrode material maintains 83% of its initial specific capacitance, demonstrating exceptional long-term electrochemical stability. The material's strong structural integrity and capacity to tolerate multiple redox processes without suffering appreciable deterioration are highlighted by this high capacitance retention. Since stable cycle performance guarantees consistent performance over long operating periods, it is an essential metric for realistic energy storage applications.

5. Conclusion

Bismuth oxide has a significant impact on the structural, optical, and electrochemical properties of vanadium Pentoxide which positions it as a highly efficient electrode material for the future supercapacitors. XRD analysis confirmed that the orthorhombic phase of V_2O_5 was retained after Bi_2O_3 with obvious lattice defects that led to the enhancement of structural stability. The XPS spectra also pointed to the presence of oxygen vacancies and a mixture of vanadium oxidation states, both of which are very useful for increasing electrical conductivity and redox activity. When Bi–O related vibrations and lattice distortions appeared, complementary FT-IR and Raman studies showed that Bi had successfully integrated into the V_2O_5 lattice. The electrical structure can be tuned through controlled composite, as demonstrated by optical tests that revealed a progressive change in band gap energies with increasing Bi concentration. Electrochemical studies validated the significant impact of Bi_2O_3 on charge storage performance. The 15% Bi_2O_3/V_2O_5 nanocomposite electrode demonstrated exceptional cycling durability with the largest specific capacitance (487 F g^{-1} at 1 A g^{-1}), higher rate capability,

and outstanding retention of 89% after 5000 cycles among the investigated concentrations. Improved ionic transport channels were confirmed by electrochemical impedance spectroscopy (EIS), which also showed decreased charge transfer resistance. Furthermore, exceeding a number of previously documented V_2O_5 - based systems, the built asymmetric device with 15% Bi_2O_3/V_2O_5 nanocomposite and activated carbon attained an exceptional energy density of 38.4 Wh kg^{-1} and a power density of 16,000 W kg^{-1}.

References

[1] G.P. Awasthi, M.B. Poudel, M. Shin, K.P. Sharma, H.J. Kim, C. Yu, Facile synthesis of a copper oxide/molybdenum disulfide heterostructure for asymmetric supercapacitors of high specific energy. Journal of Energy Storage, 42, (2021) 103140. https://doi.org/10.1016/j.est.2021.103140

[2] J. Yesuraj, T.G. Senthamaraikannan, D.H. Lim, K. Kim, Construction of ternary $Zn_{0.5}Cu_{0.5}Co_2O_4$ spinel structure on nickel foam: A comprehensive theoretical and experimental study from single to ternary metal oxides for high-energy-density asymmetric supercapacitor application. Small, 21, (2025) e2407608. https://doi.org/10.1002/smll.202407608

[3] O. Yaldır, S. Karabiberoglu, C.C. Koçak, E. Yavuz, K.V. Özdokur, Z. Dursun, Solvothermal synthesis of ZnV_2O_6/g-C_3N_4 composites for high-performance supercapacitors. Diamond and Related Materials, 157, (2025) 112544. https://doi.org/10.1016/j.diamond.2025.112544

[4] A.G. Temam, A. Alshoaibi, S.A. Getaneh, C. Awada, A.C. Nwanya, P.M. Ejikeme, F.I. Ezema, Recent progress on V_2O_5 based electroactive materials: Synthesis, properties, and supercapacitor application. Current Opinion in Electrochemistry, 38, (2023) 101239. https://doi.org/10.1016/j.coelec.2023.101239

[5] N. Shah, H. Nawaz, S.M. Abbas, A. Khesro, K. Ullah, Enhanced electrochemical properties of (V_2O_5/GO) composite electrodes for high-performance supercapacitor applications. Journal of Materials Research, 38, (2023) 2018–2029. https://doi.org/10.1557/s43578-023-00936-8

[6] Y.W. Zhang, P.P. Cheng, J.-M. Liang, W.Y. Tan, Y. Min, Morphology control of the perovskite thin films via the surface modification of nickel oxide nanoparticles layer using a bidentate chelating ligand 2,2'-Bipyridine. Synthetic Metals, 258, (2019) 116197. https://doi.org/10.1016/j.synthmet.2019.116197

[7] C. de Oliveira, F. Sigoli, I. Mazali, Property tuning through fine size control and hierarchical nanostructuring of metal oxide nanoparticles supported in porous matrices: A review. Journal of the Brazilian Chemical Society, 35(11), (2024) e-20240081. https://doi.org/10.21577/0103-5053.20240081

[8] B. Liu, K. Jiang, K. Zhu, X. Liu, K. Ye, J. Yan, G. Wang, D. Cao, Conjugated Polymer/Graphene composite as conductive Agent-Free electrode materials towards High-Performance lithiumion storage. Journal of Colloid and Interface Science, 626, (2022) 710–718. https://doi.org/10.1016/j.jcis.2022.06.090

[9] Y. Yu, G. Zhu, Q. Zhang, M. Behzadnia, Z. Yang, Y. Liu, J. Xie, Multinonmetal-doped V_2O_5 nanocomposites for lithium-ion battery cathodes. ACS Applied Energy Materials, 7, (2024) 11031–11037. https://doi.org/10.1021/acsaem.4c02043

[10] M.H. Kabir, M.Z. Hossain, M.A. Jalil, S. Ghosh, M.M. Hossain, M.A. Ali, M.U. Khandaker, D. Jana, M.M. Rahman, M.K. Hossain, J. Chowdhury, M. Kazi, M.M. Uddin, The efficacy of rare-earth doped V_2O_5 photocatalyst for removal of pollutants from industrial wastewater. Optical Materials, 147, (2024) 114724. https://doi.org/10.1016/j.optmat.2023.114724

[11] A.M. El Sayed, A.A. Abdelaziz, E.M. El-Moghazy, S.Z. Mohamed, Tuning the structural and optical features of V_2O_5 nanostructured films by Bi-doping and γ-irradiation for smart window applications. Radiation Physics and Chemistry, 232, (2025) 112620. https://doi.org/10.1016/j.radphyschem.2025.112620

[12] T.P. Jaya, P. Jayaram, T. Ramachandran, P. Hajira, C.N. Anumol, P.P. Pradyumnan, Synthesis of solid solutions of Mn and Bi substituted V_2O_5 and substitutional effect in structural and optoelectronic behavior. Physica B: Condensed Matter, 407, (2012) 1214–1218. https://doi.org/10.1016/j.physb.2012.01.098

[13] P. Falun, L. Ngamwongwan, S. Singsen, M. Chotsawat, P. Komen, A. Junkaew, S. Suthirakun, Enhancing V_2O_5 cathode performance through heterostructure engineering with the $Ti_3C_2O_2$ MXene: A computational study. The Journal of Physical Chemistry C, 128, (2024) 10774–10783. https://doi.org/10.1021/acs.jpcc.3c08078

[14] H. Barkouch, H. Bessbousse, M. Amar, S.M. Bouzzine, M. Hamidi, M.A. El Mhammedi, O.T. Alaoui, Bismuth-doped TiO_2 enable solar photocatalytic water treatment. Optical Materials, 146, (2023) 114507. https://doi.org/10.1016/j.optmat.2023.114507

[15] E. Bouzaiene, F.I.H. Rhouma, A. Haouas, K. Khirouni, J. Dhahri, Bi-doped ZnO nanoparticles: enhanced structural and dielectric properties for device applications. Journal of Sol-Gel Science and Technology, 114, (2025) 365–385. https://doi.org/10.1007/s10971-025-06693-w

[16] M.V. Arularasu, P. Vinitha, V. Vetrivelan, M.Y.

Begum, A. Siddiqua, Ce Doped V_2O_5 nanoparticles for dual functionality: Photocatalytic degradation of organic dye and supercapacitor applications. Materials Research Bulletin, 186, (2025) 113335. https://doi.org/10.1016/j.materresbull.2025.113335

[17] Y. Xie, H. Wu, J. Luo, S. Zhang, L. Wang, X. Wang, Y. Ma, P. Ning, Phase transition guided V_2O_5/β-Bi_2O_3 Z-scheme heterojunctions for efficient photocatalytic Hg0 oxidation. Separation and Purification Technology, 330, (2024) 125318. https://doi.org/10.1016/j.seppur.2023.125318

[18] S.V.P. Vattikuti, Anil Kumar Reddy Police, J. Shim, C. Byon, in situ fabrication of the Bi_2O_3–V_2O_5 hybrid embedded with graphitic carbon nitride nanosheets: Oxygen vacancies mediated enhanced visible-light–driven photocatalytic degradation of organic pollutants and hydrogen evolution. Applied Surface Science, 447, (2018) 740–756. https://doi.org/10.1016/j.apsusc.2018.04.040

[19] Y. Singh Thakur, A. Deep Acharya, S. Sharma, S. Bisoyi, Bhawna, Enhanced electrochemical performance of in situ polymerized V_2O_5-PANI nanocomposites and its practical application confirmation by assembling ionic liquid as well as solid state-based supercapacitor device. Results in Chemistry, 7, (2024) 101259. https://doi.org/10.1016/j.rechem.2023.101259

[20] K. Li, Y. Zhang, J. Jia, L. Zheng, B. Li, X. Li, T. Zhang, X. Feng, G. Liu, 2D/2D carbon nitride/Zn-doped bismuth vanadium oxide S-scheme heterojunction for enhancing photocatalytic CO_2 reduction into methanol. Industrial & Engineering Chemistry Research, 62(13), (2023) 5552-5562. https://doi.org/10.1021/acs.iecr.2c03536

[21] A. Badreldin, M.D. Imam, Y. Wubulikasimu, K. Elsaid, A.E. Abusrafa, P.B. Balbuena, A. Abdel-Wahab, Surface microenvironment engineering of black V_2O_5 nanostructures for visible light photodegradation of methylene blue. Journal of Alloys and Compounds, 871, (2021) 159615. https://doi.org/10.1016/j.jallcom.2021.159615

[22] S. Sivakumar, Y. Robinson, N.A. Mala, Studies on photocatalytic performance and supercapacitor applications of undoped and Cu-doped ZnO nanoparticles. Applied Surface Science Advances, 12, (2022) 100344. https://doi.org/10.1016/j.apsadv.2022.100344

[23] L. Xing, H. Chen, X. Wen, W. Zhou, K. Xiang, High performance of co-doped V_2O_5 cathode material in V_2O_5-saturated $(NH_4)_2SO_4$ electrolyte for ammonium ion battery. Journal of Alloys and Compounds, 925, (2022) 166652. https://doi.org/10.1016/j.jallcom.2022.166652

[24] H. Yu, X. Rui, H. Tan, J. Chen, X. Huang, C. Xu, W. Liu, D.Y.W. Yu, H.H. Hng, H.E. Hoster, Q. Yan, Cu doped V_2O_5 flowers as cathode material for high-performance lithium ion batteries. Nanoscale, 5, (2013) 4937–4943. https://doi.org/10.1039/c3nr00548h

[25] A.G. Temam, S.A. Getaneh, A. Alshoaibi, C. Awada, A.C. Nwanya, F.I. Ezema, P.M. Ejikeme, Effect of synthesis method on electrochemical activities of V_2O_5 nanoparticles for supercapacitor application. Journal of Materials Science: Materials in Electronics, 36, (2025). https://doi.org/10.1007/s10854-025-14816-w

[26] X. Liu, C. Liu, Z. Wang, H. Chen, Z. Liu, J. Yang, W.-M. Lau, D. Zhou, Facile hydrothermal synthesis of V_2O_5 nanofibers as cathode material for aqueous zinc-ion batteries. Journal of Alloys and Compounds, 896, (2022) 163071. https://doi.org/10.1016/j.jallcom.2021.163071

[27] M. Jayachandran, A. Rose, T. Maiyalagan, N. Poongodi, T. Vijayakumar, Effect of various aqueous electrolytes on the electrochemical performance of V_2O_5 spindle-like nanostructures as electrode material for supercapacitor application. Journal of Materials Science: Materials in Electronics, 32, (2021) 6623–6635. https://doi.org/10.1007/s10854-021-05378-8

[28] J. Mu, J. Wang, J. Hao, P. Cao, S. Zhao, W. Zeng, B. Miao, S. Xu, Hydrothermal synthesis and electrochemical properties of V_2O_5 nanomaterials with different dimensions. Ceramics International, 41, (2015) 12626–12632. https://doi.org/10.1016/j.ceramint.2015.06.091

[29] D. Lohita, H.P. Kavitha, Development of ZrO_2, V_2O_5 co-doped carbon nanosheets from green and template-free method for supercapacitor applications. Journal of Alloys and Compounds, 962, (2023) 170862. https://doi.org/10.1016/j.jallcom.2023.170862

[30] S. Muthamizh, M. Shahadat Hossain, A. Alsulmi, R.R. Macadangdang Jr, S. Sambasivam, K. Arul Varman, Design and construction of heterostructured $Zn_2V_2O_7$ cubes and hexagons as an electrode material for high-performance asymmetric supercapacitor applications. Journal of Colloid and Interface Science, 660, (2024) 215–225. https://doi.org/10.1016/j.jcis.2024.01.083

[31] P. Jency Sebatine, R.B. Shivani, S. Sherin Celshia, S. Muthamizh, K. Arul varman, K. Shanmugaraj, R. Mohan Kumar, Fabrication of NiO/ V_2O_5 nanocomposite as photocatalyst for cationic dye degradation and its pathway. Ceramics International, 51(26), (2025) 50516-50529. https://doi.org/10.1016/j.ceramint.2025.08.282

[32] M. Taha, E.L.H. Mayes, M.R. Field, M. Sun, M. Singh, W. Zou, Room-temperature application of VO_2 microstructures on rigid and flexible substrates based on synthesis of crystalline VO_2 solution. Materials Advances, 1(6), (2020) 1685-1694. https://doi.org/10.1039/d0ma00338g

[33] Q. Ren, N. Qin, B. Liu, Y. Yao, X. Zhao, Z. Deng, Y. Li, Y. Dong, D. Qian, B.-L. Su, W. Zhang, H.-E. Wang, An oxygen-deficient vanadium oxide@N-doped carbon heterostructure for sodium-ion batteries: insights into the charge storage mechanism and enhanced reaction kinetics. Journal of Materials Chemistry A, 8, (2020) 3450–3458. https://doi.org/10.1039/c9ta11965e

[34] M. Mazidi, R.M. Behbahani, A. Fazeli, Ce promoted V_2O_5 catalyst in oxidation of SO_2 reaction. Applied Catalysis B: Environmental, 209, (2017) 190–202. https://doi.org/10.1016/j.apcatb.2017.02.034

[35] C. Youn, W. Ko, A. Cho, J. Lee, S.Y. Yeo, Y. Seo, J. Lee, B.-S. Lee, J. Kim, T. Choi, One-dimensional nanostructured vanadium oxides with single-crystalline structure synthesized by cellulose nanocrystal-template-assisted hydrothermal method for Li-ion battery cathodes. Cellulose, 30, (2023) 7177–7191. https://doi.org/10.1007/s10570-023-05325-2

[36] M. Selvamani, D. Elangovan, A. Alsalme, A.V. Kesavan, G. Ayyakannu Sundaram, A. Santhana Krishna Kumar, $Bi_2W_2O_9$ nanoflakes synthesized via a hydrothermal method: Antibacterial potency and cytotoxicity evaluation on human dermal fibroblasts. ACS Omega 10(6), (2025) 5468–5477. https://doi.org/10.1021/acsomega.4c07612

[37] S. Balachandran, K.J. Jothi, S. Muthamizh, A. Subhasri, R.D. Kumar, A.S.K. Kumar, M.A. Wadaan, H. Chengzhi, Facile fabrication of $BiVO_4$ Microspheres: Investigating their twin application on potential in electrochemical capacitors and protein detection. Journal of Power Sources, 650, (2025) 237481. https://doi.org/10.1016/j.jpowsour.2025.237481

[38] D.N. Le, T.A. Le, T.P. Ho Le, C.M. Dang, P.H. Tu, Y. Shiratori, T. Chanh Duc Doan, Morphology evolution of Fe-doped V_2O_5 flower-like microspheres for H_2S adsorption. Materials Chemistry and Physics, 335, (2025) 130541. https://doi.org/10.1016/j.matchemphys.2025.130541

[39] M.R. da S. Pelissari, N.F. Azevedo Neto, L.P. Camargo, L.H. Dall'Antonia, Characterization and photo-induced electrocatalytic evaluation for $BiVO_4$ films obtained by the SILAR process. Electrocatalysis, 12, (2021) 211–224. https://doi.org/10.1007/s12678-021-00641-2

[40] N. Sharma, Z. Pap, I. Székely, M. Focsan, G. Karacs, Z. Nemeth, S. Garg, K. Hernadi, Combination of iodine-deficient BiOI phases in the presence of CNT to enhance photocatalytic activity towards phenol decomposition under visible light. Applied Surface Science, 565, (2021) 150605. https://doi.org/10.1016/j.apsusc.2021.150605

[41] S.H. Lee, H.M. Cheong, M. Je Seong, P. Liu, C.E. Tracy, A. Mascarenhas, J.R. Pitts, S.K. Deb, Microstructure study of amorphous vanadium oxide thin films using raman spectroscopy. Journal of Applied Physics, 92, (2002) 1893–1897. https://doi.org/10.1063/1.1495074

[42] B.O. Orimolade, O.A. Arotiba, Bismuth vanadate in photo electrocatalytic water treatment systems for the degradation of organics: A review on recent trends. Journal of Electroanalytical Chemistry, 878, (2020) 114724. https://doi.org/10.1016/j.jelechem.2020.114724

[43] K. Pradeeswari, A. Venkatesan, P. Pandi, K.G. Prasad, K. Karthik, T. Maiyalagan, R.M. Kumar, Effect of cerium on electrochemical properties of V_2O_5 nanoparticles synthesized via non-aqueous sol-gel technique, Ionics (Kiel), 26, (2020) 905–912. https://doi.org/10.1007/s11581-019-03259-z

[44] L. Niu, Z. Li, Y. Xu, J. Sun, W. Hong, X. Liu, J. Wang, S. Yang, Simple synthesis of amorphous $NiWO_4$ nanostructure and its application as a novel cathode material for asymmetric supercapacitors. ACS Applied Materials & Interfaces, 5, (2013) 8044–8052. https://doi.org/10.1021/am402127u

[45] N. Wang, Y. Zhang, T. Hu, Y. Zhao, C. Meng, Facile hydrothermal synthesis of ultrahigh-aspect-ratio V_2O_5 nanowires for high-performance supercapacitors. Current Applied Physics, 15, (2015) 493–498. https://doi.org/10.1016/j.cap.2015.01.026

[46] V. Mounasamy, M. Keerthana, N. Ponpandian, Exploring the enhanced electrochemical activity of V_2O_5/h-BN: Investigating its structural dynamics for asymmetric supercapacitors. ACS Applied Electronic Materials, 6(8), (2024) 5681-5693. https://doi.org/10.1021/acsaelm.4c00709

[47] A.J. Lovett, M.P. Wells, Z. He, J. Lu, H. Wang, J.L. MacManus-Driscoll, High ionic conductivity in fluorite δ-bismuth oxide-based vertically aligned nanocomposite thin films. Journal of Materials Chemistry A, 10, (2022) 3478–3484. https://doi.org/10.1039/d1ta07308g

[48] W. Ma, H. Nan, Z. Gu, B. Geng, X. Zhang, Superior performance asymmetric supercapacitors based on $ZnCo_2O_4$@MnO_2core–shell electrode. Journal of Materials Chemistry A, 3, (2015) 5442–5448. https://doi.org/10.1039/c5ta00012b

[49] J. Yan, Z. Fan, W. Sun, G. Ning, T. Wei, Q. Zhang, R. Zhang, L. Zhi, F. Wei, Advanced asymmetric supercapacitors based on $Ni(OH)_2$/graphene and porous graphene electrodes with high energy density. Advanced Functional Materials, 22(12), (2012) 2632–2641. https://doi.org/10.1002/adfm.201102839

[50] F. Lu, M. Zhou, W. Li, Q. Weng, C. Li, Y. Xue, X. Jiang, X. Zeng, Y. Bando, D. Golberg,

Engineering sulfur vacancies and impurities in $NiCo_2S_4$ nanostructures toward optimal supercapacitive performance. Nano Energy, 26, (2016) 313–323. https://doi.org/10.1016/j.nanoen.2016.05.042

[51] B. Saravanakumar, K.K. Purushothaman, G. Muralidharan, Interconnected V_2O_5 nanoporous network for high-performance supercapacitors. ACS Applied Materials & Interfaces, 4(9), (2012) 4484–4490. https://doi.org/10.1021/am301162p

[52] H. Liu, W. Zhu, D. Long, J. Zhu, G. Pezzotti, Porous V_2O_5 nanorods/reduced graphene oxide composites for high performance symmetric supercapacitors. Applied Surface Science, 478, (2019) 383–392. https://doi.org/10.1016/j.apsusc.2019.01.273

[53] A. Ray, A. Roy, P. Sadhukhan, S.R. Chowdhury, P. Maji, S.K. Bhattachrya, S. Das, Electrochemical properties of TiO_2-V_2O_5 nanocomposites as a high performance supercapacitors electrode material. Applied Surface Science, 443, (2018) 581–591. https://doi.org/10.1016/j.apsusc.2018.02.277

[54] D. Govindarajan, V. Uma Shankar, R. Gopalakrishnan, Supercapacitor behavior and characterization of RGO anchored V_2O_5 nanorods. Journal of Materials Science: Materials in Electronics, 30, (2019) 16142–16155. https://doi.org/10.1007/s10854-019-01984-9

[55] S. Sutrave, S. Konda, D. Velpula, S.A. Volety, S.R. Ravula, S.C. Chidurala, B.N. Tumma, A simple solution combustion method for the synthesis of V_2O_5 nanostructures for supercapacitor applications. Applied Surface Science Advances, 12, (2022) 100331. https://doi.org/10.1016/j.apsadv.2022.100331

[56] B. Saravanakumar, K.K. Purushothaman, G. Muralidharan, High performance supercapacitor based on carbon coated V_2O_5 nanorods. Journal of Electroanalytical Chemistry, 758, (2015) 111–116. https://doi.org/10.1016/j.jelechem.2015.10.031

[57] C. Xia, Q. Jiang, C. Zhao, P.M. Beaujuge, H.N. Alshareef, Asymmetric supercapacitors with metal-like ternary selenides and porous graphene electrodes. Nano Energy, 24, (2016) 78–86. https://doi.org/10.1016/j.nanoen.2016.04.012

[58] J. Yesuraj, J. Kim, R. Yang, K. Kim, Deoxyribonucleic acid scaffolded and encapsulated one-dimensional gadolinium (III) hydroxide nanorods for supercapacitors and oxygen evaluation reaction properties. Advanced Composites and Hybrid Materials, 7, (2024). https://doi.org/10.1007/s42114-024-00881-y

[59] G. Sun, H. Ren, Z. Shi, L. Zhang, Z. Wang, K. Zhan, Y. Yan, J. Yang, B. Zhao, V_2O_5/vertically-aligned carbon nanotubes as negative electrode for asymmetric supercapacitor in neutral aqueous electrolyte. Journal of Colloid and Interface Science, 588, (2021) 847–856. https://doi.org/10.1016/j.jcis.2020.11.126

[60] Q.T. Qu, Y. Shi, L.L. Li, W.L. Guo, Y.P. Wu, H.P. Zhang, S.Y. Guan, R. Holze, $V_2O_5 \cdot {}_{0.6}H_2O$ nanoribbons as cathode material for asymmetric supercapacitor in K_2SO_4 solution. Electrochemistry communications, 11(6), (2009) 1325–1328. https://doi.org/10.1016/j.elecom.2009.05.003

[61] H. Jiang, H. Niu, X. Yang, Z. Sun, F. Li, Q. Wang, F. Qu, Flexible Fe_2O_3 and V_2O_5 nanofibers as binder-free electrodes for high-performance all-solid-state asymmetric supercapacitors. Chemistry–A European Journal, 24, (2018) 10683–10688. https://doi.org/10.1002/chem.201800461

[62] Z.-Q. Hou, Z.-G. Yang, Y.-P. Gao, Synthesis of vanadium oxides nanosheets as anode material for asymmetric supercapacitor. Chemical Papers, 72, (2018) 2849–2857. https://doi.org/10.1007/s11696-018-0504-9

Authors Contribution Statement

P. Jency Sebatine: Formal analysis, Methodology, Writing – Original draft, Investigation. R. Mohan Kumar: Conceptualization, Supervision, Writing – Review & editing. S. Sherin Celshia: Resources, Software. K. Arul varman: Resources, Software. S. Muthamizh: Formal analysis, Methodology, Writing – Original draft, Investigation. All the authors read and approved the final version of the manuscript.

Funding

The authors declare that no funds, grants or any other support were received during the preparation of this manuscript.

Declaration of generative AI and AI-assisted technologies in the manuscript preparation process

During the preparation of this work, the authors used QuillBot and ChatGPT for the English language correction. After using this tool, the authors reviewed and edited the content as needed and take(s) full responsibility for the content of the published article.

Competing Interests

The authors declare that there are no conflicts of interest regarding the publication of this manuscript.

Data Availability

The data supporting the findings of this study can be obtained from the corresponding author upon reasonable request.

Has this article screened for similarity?

Yes

About the License